

## DISSIPATIONLESS COLLAPSE IN AN EXPANDING UNIVERSE

NEAL KATZ<sup>1</sup>

Princeton University Observatory

Received 1989 October 13; accepted 1990 July 27

### ABSTRACT

The formation and equilibrium characteristics of systems formed through dissipationless collapse are studied. Initially, the systems are isolated, spherically symmetric top hats in solid body rotation and in Hubble flow. Small-scale power is added using the Zel'dovich approximation assuming a power-law slope and including velocities self-consistently. Simulations are run for two different values of the power-law slope:  $n = 0$  and  $n = -2.5$ . The initial conditions are more general than past simulations of isolated systems and are chosen to be more cosmologically relevant in an effort to connect simulations involving the collapse of isolated perturbations with those extracted from larger cosmological simulations.

With these initial conditions collapses are clumpy and resemble multiple merger events. The final density profiles in projection approximately follow a de Vaucouleurs  $R^{1/4}$  law. The radial orbit instability does not appear important in determining the final shape of the systems. These shapes range from oblate to triaxial to prolate. With these more general initial conditions the initial  $T/W$  does not completely determine the final equilibrium state. The equilibrium systems are slowly rotating, with a measured flat rotation curve, and are supported by an anisotropic velocity dispersion. The final equilibria closely resemble elliptical galaxies with projected ellipticities ranging from E1 to E6. This lends support to the theory that elliptical galaxies formed through dissipationless collapse. These models could also represent formation of galactic halos and give new insights into the central structure of dark halos.

*Subject headings:* cosmology — galaxies: clustering — galaxies: formation — galaxies: structure

### 1. INTRODUCTION

The study of dissipationless collapse has a long history (Hénon 1964; Peebles 1970; Bouvier & Janin 1970; Gott 1973). Traditionally, studies considered the collapse of isolated top-hat perturbations with Poisson initial conditions. Such simulations have recently been studied in more detail by many authors, e.g., van Albada (1982), McGlynn (1984), Aguilar, Merritt, & Duncan (1987), Aguilar & Merritt (1989). They are primarily interested in the formation of elliptical galaxies so they assume that the dissipationless material is stellar. The difficulty with these earlier simulations is that they adopt unrealistic initial conditions. Initial particle velocities in these calculations are selected from a Gaussian distribution without regard for the inhomogeneities present in the initial particle distribution. Such a velocity field would probably not have arisen in any cosmogony. Most likely, clumpiness in the mass distribution would gravitationally induce motions in the particles correlated with the initial clump distribution. Furthermore, since the particles are initially distributed in a Poisson manner with the possible ad hoc addition of clumps (e.g., van Albada 1982; McGlynn 1984), there is no control over the amplitude of the Poisson small-scale power, which consequently depends only on the number of particles. This method also lacks a way to quantify the small-scale power when clumps are added.

Other authors (Quinn, Salmon, & Zurek 1986, Frenk et al. 1988; Barnes & Efstathiou 1987; Quinn & Zurek 1988; Zurek, Quinn, & Salmon 1988) have studied dissipationless collapses by examining subregions of larger cosmological simulations. These calculations address the formation of galactic halos, so

the dissipationless material represents some form of dark matter. Unfortunately, these results generally suffer from poor resolution since the halos are not well sampled.

This paper considers the collapse of isolated top-hat perturbations, but with more general and cosmologically relevant initial conditions. The simulations are started in Hubble flow with varying amounts of solid body rotation and small-scale power that is added in a controlled manner, with different power-law slopes and amplitudes. Velocities are initialized under the assumption that they were acquired solely through gravitational interaction before the start of the simulation, in a manner consistent with the clumpiness of the particle distribution. Eighteen collapses are studied in all. These models are an attempt to bridge the gap between the two classes of simulations mentioned above and will also be compared to future dissipative collapse simulations.

These simulations have been made possible through the recent development of hierarchical tree codes—a new class of efficient  $N$ -body techniques (Barnes & Hut 1986; Hernquist 1987). The subclumps that form during collapse would not be adequately resolved with multipole codes used in past studies (e.g., van Albada 1982; McGlynn 1984, Aguilar & Merritt 1989), and direct summation is too slow to allow the use of enough particles to give adequate resolution. The efficiency of the integrations has been further increased by the incorporation of individual particle time steps.

Section 2 discusses the code used in the present study, the method for generating initial conditions, the different sets of initial conditions which are evolved, and the method used to determine the shapes of the equilibrium systems. Section 3 presents details of the collapses, while § 4 discusses their implications. Section 5 gives a brief summary of the major conclusions.

<sup>1</sup> Postal address: Steward Observatory, University of Arizona, Tucson, AZ 85721.

## 2. METHODS

2.1. *N-Body Code*

The simulations are run with a hierarchical tree code based on the Barnes-Hut algorithm (Barnes & Hut 1986) including quadrupole terms. Unlike multipole expansion codes, tree algorithms do not impose any global geometry on the system. Furthermore, the present version of the Barnes-Hut algorithm dynamically resolves the formation and subsequent merger of subclumps that occur during the collapse, making it ideal for studying collapse problems. Direct summation codes also have this advantage, but with computation cost scaling as  $O(n^2)$  per time step as opposed to  $O(n \ln n)$  for tree codes. The improved efficiency allows tree codes to run with larger numbers of particles, and correspondingly higher resolution than direct summation methods.

Unlike previous implementations of the Barnes-Hut algorithm, the particles in the simulations here are advanced with individual time-steps. Each particle is advanced with a time step that is a power of two subdivision of the fixed system time step. Particles can always move to a smaller time step, but may move to a larger time step only if it is synchronized with their own time step. This ensures that the system will be time synchronized at the end of every system time step. Care must be taken to maintain the second-order accuracy of the leapfrog integrator when particles change time step. Details of this procedure are presented in Hernquist & Katz (1989, hereafter HK). The use of individual particle time steps allows the system to be integrated more accurately in a given amount of CPU time than for fixed time steps. During a typical simulation, particles are distributed nearly uniformly in time steps ranging from the largest system time step to a time step one-sixteenth this size.

Each particle's time step is chosen using an energy criterion. A particle's time step,  $\Delta t_i$ , is adjusted such that

$$a_i v_i \Delta t_i \leq e_{\text{tot}} E_i, \quad (1)$$

where  $a_i$  is the acceleration,  $v_i$  is the velocity, and  $e_{\text{tot}}$  is a parameter that determines the fractional accuracy of the integrations (Ewell 1988). In the simulations presented here,  $e_{\text{tot}} = 0.1$ . The energy,  $E_i$  used in the time-step adjustment criterion, is usually taken to be the binding energy per unit mass of the individual particle. This choice can fail with realistic cosmological initial conditions, since many particles near the edge of a perturbation have nearly zero binding energy and would be given small time steps even though the potential is varying slowly there. To remedy this problem,  $E_i$  is chosen to be  $\max(E_k, E_p/6)$  for all the particles, where  $E_k$  and  $E_p$  are the mean kinetic energy per unit mass and the mean potential energy per unit mass of the system (Ewell 1988).

Unlike most *N*-body codes that soften gravitational interactions using a Plummer density profile, the tree code used in these simulations softens particles using a spline kernel (HK). This form of softening is attractive since the density profile has compact support, and the acceleration is identical to the Kepler form for  $r \geq 2\epsilon$ , where  $\epsilon$  is the softening length. These properties are particularly advantageous for hierarchical tree codes, since the multipole expansions used to represent the potentials of distant cells in the tree structure assume that the bodies are point particles of finite size. In the simulations here, the gravitational softening length is  $\epsilon = 0.06$ , which is about the mean interparticle separation at the half mass radius in the

equilibrium systems. This choice reduces the effects of two-body relaxation.

The present code vectorizes fully on most supercomputers (HK; Hernquist 1990). The simulations use of order 4000 particles and require  $\sim 45$  CPU minutes to run on a CRAY YMP for 700 system time steps, corresponding to about seven collapse times. The energy is conserved to better than 0.3% in all the runs except for the coldest one, in which energy is conserved to only 0.5%. All computations here are performed at the Pittsburgh Supercomputing Center.

2.2. *Initial Conditions*

The purpose of the current simulations is to model the dissipationless collapse of an isolated object with cosmologically relevant initial conditions. Since it is not possible to represent a large volume of the universe and still resolve subgalactic scales with only 4000 particles, several compromises have to be made. The objects are taken to be perturbed homogeneous spheres expanding with the Hubble flow with vacuum boundary conditions. Since tidal interactions are not included, the systems are started in solid body rotation to give them some angular momentum. Finally, small-scale noise is added to the homogeneous spheres, in accord with cosmologically relevant power spectra.

The systems are set up in the following manner. First, particles are placed on a cubic lattice with periodic boundaries. The particles are then perturbed from the lattice and assigned self-consistent peculiar velocities using the Zel'dovich approximation (Zel'dovich 1970) assuming a power spectrum with spectral index  $n$ . In addition, a cosine cutoff is applied to the power-law spectrum at the Nyquist frequency. Particles within a sphere of unit radius are then extracted for the simulations. The original lattice is constructed so that this sphere contains  $\sim 4000$  particles. Particles are assigned equal masses, normalized so that the total system mass is 0.9091, the mass fraction of dark matter in a galaxy if the dark to gaseous matter ratio is 10 to 1. Velocities are added such that the system is in Hubble flow with unit Hubble constant and in solid body rotation. Velocities and positions are then adjusted to center-of-mass coordinates.

There are three important differences between these initial conditions and those used in previous studies involving the collapse of isolated top-hat perturbations. First, the simulations here are started in an expanding Hubble flow rather than in a stationary configuration, allowing more time for substructure to develop. Second, both the amplitude and the type of small-scale noise are fully controlled, unlike other simulations that distribute the particles within the initial perturbation in an ad hoc manner. Some simply place the particles at random (van Albada 1982; Aguilar & Merritt 1989), introducing noise that is approximated by an  $n = 0$  power law but with an amplitude determined solely by the number of particles. Other authors (van Albada 1982; McGlynn 1984) put in small-scale power by arbitrarily adding clumps to the system without any knowledge of the shape or amplitude of the power spectrum on small scales. Finally, all previous simulations add the velocities randomly, ignoring inhomogeneities in the initial density field. This has the undesirable effect of reducing the growth rate of initial density perturbations and inhibiting the collapse of masses below a scale set by the magnitude of the initial velocity dispersion. This is similar to adding a Jeans mass cutoff to the power spectrum. Since smaller mass scales collapse first in  $n = 0$  (also in  $n = -2.5$ ) power spectra, mass scales slightly

larger than this Jeans mass dominate during the large-scale collapse of the system. If, on the other hand, velocities are included in a self-consistent manner, as they are here, all mass scales can collapse as the system evolves. Also, when self-consistent velocities are used, clumpier collapses are actually warmer than the smoother collapses.

In this paper two suites of models are considered: one has power-law slope  $n = 0$ , equivalent to Poisson noise, and the other has slope  $n = -2.5$ , similar to cold dark matter spectra if the system mass is close to that of galaxies (Peebles 1982). Runs are performed with initial angular rotation velocities,  $\omega$ , of 0.1, 0.2, and 0.4. These correspond to  $\lambda$ 's of 0.02, 0.04, and 0.08, respectively, where

$$\lambda \equiv \frac{J|E|^{1/2}}{GM^{5/2}} \quad (2)$$

is the dimensionless spin parameter used to characterize the amount of angular momentum in bound systems (Peebles 1971). Here  $J$  is the total angular momentum of the system,  $E$  the binding energy,  $M$  the total mass, and following standard convention, the gravitational constant,  $G$  is set equal to 1 throughout. Three different amplitudes for the small-scale power are used, separated by factors of 2 making a total of nine different initial conditions for each  $n$ . Amplitudes are normalized to the  $k = 1$  mode of the system, and phases are chosen to be identical for all the simulations. Scaling to a system of units with mass unit  $7 \times 10^{11} M_{\odot}$ , implying a system mass of  $6.4 \times 10^{11} M_{\odot}$ , and length unit 62.5 kpc, and assuming that  $H_0 = 50 \text{ km s}^{-1} \text{ Mpc}$  and  $\Omega = 1$ , allows the three amplitudes of small-scale power to be compared with equivalent cold dark matter amplitudes. In the cold dark matter model, the amplitude of the spectrum is characterized by the bias parameter,  $b$ , defined as the ratio between fluctuations in the galaxy distribution and the density distribution (Frenk et al. 1990). When normalized to the observed galaxy correlation length, the amplitude scales as  $1/b$ . The model with lowest amplitude corresponds to a  $b = 4$  amplitude, when normalized to the  $k = 1$  mode. The next highest corresponds to a  $b = 2$  amplitude and the highest corresponds to an unbiased amplitude (i.e.,  $b = 1$ ). Using the same normalization for the radius and mass as above and assuming the same values for  $H_0$  and  $\Omega$ , the initial over-density of the system is 0.32. This corresponds to a  $(1.34b)\sigma$  peak in the CDM spectrum when filtered with a top hat of mass  $6.4 \times 10^{11} M_{\odot}$ . Details of the initial conditions are given in Table 1, top, for  $n = 0$  models and in Table 1, bottom, for  $n = -2.5$  models. In the tables,  $T_{\text{rand}}$  refers to the kinetic energy introduced by clumpiness and  $T_{\text{rot}}$  refers to kinetic energy introduced by the solid body rotation. Since the simulations are initially expanding, the potential energy,  $W$ , is the formal value at maximum expansion, i.e., the initial  $W$  plus the initial expansion energy. Note that  $T_{\text{rand}}/W$  is smaller for the same amplitude of small-scale power in the  $n = -2.5$  models than in the  $n = 0$  models, since the amount of power decreases rapidly at small scales when  $n = -2.5$ . With  $n = 0$ , however, the amount of power remains constant at smaller mass scales.

### 2.3. Determining Shapes

Determining the shape of a three-dimensional distribution of particles is a difficult task. Ideally, one would like to find the shapes of isodensity surfaces, but with  $\sim 4000$  particles, only the axis ratios can be measured accurately. The ratios  $b/a$  and  $c/a$  are computed from the principal moments of inertia, and

TABLE 1  
INITIAL CONDITIONS

Run	$\omega$	$b$	$T_{\text{rot}}/W$	$T_{\text{rand}}/W$	$T/W$
$n = 0$					
1a	0.1	4	$8.16 \times 10^{-3}$	$7.49 \times 10^{-4}$	$8.91 \times 10^{-3}$
2a	0.1	2	$8.28 \times 10^{-3}$	$3.02 \times 10^{-3}$	$1.13 \times 10^{-2}$
3a	0.1	1	$8.21 \times 10^{-3}$	$1.18 \times 10^{-2}$	$2.00 \times 10^{-2}$
4a	0.2	4	$3.26 \times 10^{-2}$	$7.49 \times 10^{-4}$	$3.33 \times 10^{-2}$
5a	0.2	2	$3.32 \times 10^{-2}$	$3.02 \times 10^{-3}$	$3.62 \times 10^{-2}$
6a	0.2	1	$3.28 \times 10^{-2}$	$1.18 \times 10^{-2}$	$4.46 \times 10^{-2}$
7a	0.4	4	$1.30 \times 10^{-1}$	$7.49 \times 10^{-4}$	$1.31 \times 10^{-1}$
8a	0.4	2	$1.33 \times 10^{-1}$	$3.02 \times 10^{-3}$	$1.36 \times 10^{-1}$
9a	0.4	1	$1.31 \times 10^{-1}$	$1.18 \times 10^{-2}$	$1.43 \times 10^{-1}$
$n = -2.5$					
1b	0.1	4	$8.12 \times 10^{-3}$	$1.04 \times 10^{-4}$	$8.22 \times 10^{-3}$
2b	0.1	2	$8.16 \times 10^{-3}$	$4.17 \times 10^{-4}$	$8.58 \times 10^{-3}$
3b	0.1	1	$8.36 \times 10^{-3}$	$1.69 \times 10^{-3}$	$1.00 \times 10^{-2}$
4b	0.2	4	$3.24 \times 10^{-2}$	$1.04 \times 10^{-4}$	$3.25 \times 10^{-2}$
5b	0.2	2	$3.26 \times 10^{-2}$	$4.17 \times 10^{-4}$	$3.30 \times 10^{-2}$
6b	0.2	1	$3.35 \times 10^{-2}$	$1.69 \times 10^{-3}$	$3.52 \times 10^{-2}$
7b	0.4	4	$1.30 \times 10^{-1}$	$1.04 \times 10^{-4}$	$1.30 \times 10^{-1}$
8b	0.4	2	$1.30 \times 10^{-1}$	$4.17 \times 10^{-4}$	$1.31 \times 10^{-1}$
9b	0.4	1	$1.34 \times 10^{-1}$	$1.69 \times 10^{-3}$	$1.36 \times 10^{-1}$

are defined by

$$\frac{b}{a} = \sqrt{\frac{\sum m_i y_i^2}{\sum m_i x_i^2}}, \quad (3a)$$

$$\frac{c}{a} = \sqrt{\frac{\sum m_i z_i^2}{\sum m_i x_i^2}}. \quad (3b)$$

In these expressions  $x$ ,  $y$ , and  $z$  refer to a coordinate system in which the moment of inertia tensor is diagonal ( $x$  is the long axis,  $y$  is the intermediate axis, and  $z$  is the short axis).

The major difficulty in determining the axis ratios is deciding which particles to include in the summations in equations (3a) and (3b). Of course, unbound particles are excluded, but one would like to know the shape of the system at various radii. Selecting particles within a spherical volume biases the shape unless the particle distribution is nearly spherical. Other authors (e.g., Aguilar & Merritt 1989) use a fixed percentage of the most tightly bound particles. This can also bias the computed shape, since equipotential surfaces are rounder than isodensity surfaces. Also, particles contained within collapsed subclumps in the outer parts of the system may be included in the summations and give spurious results.

To avoid some of these difficulties the following iterative procedure is used. Assume that one would like to determine the axis ratios of all particles within a distance  $d$  of the center. First, axis ratios are determined for the particles enclosed within a sphere of radius  $d$  centered on the system's center of mass using equations (3a), and (3b). Then new axis ratios are computed using just the particles contained within the ellipsoidal volume with these axis ratios and centered on the center of mass of the spherical volume. Thus, particle  $i$  is included in the summation if  $\zeta_i \leq d$ , where

$$\zeta_i^2 = x_i^2 + \left[ \frac{y_i}{(b/a)} \right]^2 + \left[ \frac{z_i}{(c/a)} \right]^2. \quad (4)$$

The procedure is then repeated for the new ellipsoidal volume (using the old ellipsoidal volume in the place of the spherical volume), and iterated until convergence is reached. Usually, convergence is reached after  $\sim 5$ – $10$  iterations to an accuracy of  $\sim 0.01\%$  in most cases and  $\sim 1\%$  in the worst cases.

### 3. RESULTS

#### 3.1. Collapses

Figure 1a shows the collapse of a system with the lowest value for the amplitude of the small-scale power considered here, and Figure 1b shows a collapse with the highest value. In both cases the angular rotation speed,  $\omega$ , is 0.2 and the slope of the power spectrum is 0. Times are shown in natural system units, and the figures measure four radius units across. To convert to physical time,  $t$ , choose a radius unit,  $R$ , and a mass unit,  $M$ , then  $t = (R^3/GM)^{1/2}$ . Figures 2a and 2b show the collapse of initially identical systems except for the slope of the power spectrum, which is now  $-2.5$ . Note that the collapses are always clumpy and resemble multiple merger events. The clumps that merge together are much denser in collapses with high rather than low amplitudes, and they retain their individual identities through several dynamical times. In the low-amplitude runs (Figs. 1b and 2b), the clumps are loosely bound puffy clouds and quickly lose their individual identities when merging. In the collapses with power-law slope  $n = -2.5$  (Figs. 2a and 2b), the objects which merge have nearly the same mass as the entire system, while in the  $n = 0$  runs (Figs. 1a and 1b), all mass scales are represented.

#### 3.2. Density Profiles

Density profiles for the 18 simulations are determined by binning the particles in concentric ellipsoidal shells with constant axis ratios computed as above, logarithmically spaced in  $\zeta$ . The axis ratios are determined at  $\zeta = 2$ , beyond which the density in the simulations declines rapidly. These density profiles are then fitted to a modified Jaffe density profile (Jaffe 1983)

$$\rho(\zeta) = \frac{CM}{4\pi(b/a)(c/a)} \frac{1}{(\zeta^2 + a_1^2)(\zeta + a_2)^2}, \quad (5a)$$

where  $M$  is the total mass of the system,  $a_1$  and  $a_2$  are constants, and

$$C = (a_1^2 + a_2^2) \left[ a_2 + \frac{a_2 a_1^2}{a_1^2 + a_2^2} \ln \frac{a_2^2}{a_1^2} - \frac{\pi a_1 (a_2^2 - a_1^2)}{2(a_1^2 + a_2^2)} \right]^{-1}. \quad (5b)$$

The fits are determined by the least squares method, weighting all points  $\zeta \leq 2$  equally and excluding all other points. The results are shown in Table 2, top, for the  $n = 0$  models and in Table 2, bottom, for the  $n = -2.5$  models. The fits are generally good, as suggested by their chi-squared estimates. Most of the larger chi-square values are the result of noise in the innermost, undersampled regions. The density profiles and their best-fit models are shown in Figure 3a for the  $n = 0$  runs and in Figure 3b for the  $n = -2.5$  runs. Generally, the density profiles for the  $n = 0$  and  $n = -2.5$  runs are quite similar. Fits attempted using a Jaffe model with  $a_1 = 0$  are found to be worse than fits with a nonzero  $a_1$  when comparing chi-square values and taking into account the use of one fewer parameter. It is also apparent that no single power law can fit the density profiles. Also shown in Table 2 are the formal half-mass radii calculated from the fitted density profiles and the estimated

TABLE 2  
MODEL FITS

Run	Mass	$a_1$	$a_2$	$\chi^2$	Half-Mass Radius	Core Radius
To $n = 0$ Runs						
1a	0.95	0.40	0.09	1.86	0.67	0.08
2a	1.06	0.65	0.08	1.05	0.93	0.07
3a	1.11	0.86	0.07	1.32	1.14	0.07
4a	0.98	0.44	0.11	0.85	0.76	0.09
5a	1.04	0.60	0.12	1.30	0.97	0.11
6a	1.28	0.16	1.27	1.58	1.68	0.13
7a	1.04	0.33	0.40	2.39	1.04	0.17
8a	1.20	1.08	0.10	3.27	1.47	0.10
9a	1.99	0.05	4.03	1.87	4.18	0.05
To $n = -2.5$ Runs						
1b	0.92	0.29	0.13	2.08	0.60	0.09
2b	1.02	0.54	0.07	1.05	0.79	0.07
3b	1.27	0.13	0.89	1.03	1.22	0.10
4b	0.91	0.29	0.14	1.65	0.62	0.10
5b	1.10	0.67	0.08	1.35	0.96	0.07
6b	1.26	0.15	0.84	1.32	1.21	0.12
7b	0.93	0.40	0.14	1.37	0.76	0.11
8b	1.13	0.77	0.12	3.14	1.17	0.11
9b	1.20	0.23	1.20	2.64	1.76	0.18

core-radii of the systems. The core radius is defined to be the radius where the logarithmic slope of the model density profile is equal to  $-1$  (see below).

Several things should be noted about the results in Table 2. The first concerns the fits themselves and the roles assumed by the parameters  $a_1$  and  $a_2$  in the different runs. In the standard Jaffe model,  $a_1$  is less than  $a_2$ . In that case,  $a_1$  defines the core-radius of the system and  $a_2$ , the radius where the logarithmic slope of the density profile changes from  $-2$  to  $-4$ , is related to the effective radius of an  $R^{1/4}$  law fit. Remember that when a Jaffe model is viewed in projection it roughly follows a de Vaucouleurs  $R^{1/4}$  law. In many of the fits here, however,  $a_1$  is greater than  $a_2$ , motivating the above definition of the core radius, and the decision to compare models at multiples of the half-mass radius. Only in the runs with the highest amplitude small-scale power and with large rotation (runs 6a, 9a, and 9b) do the models take the standard Jaffe form.

Other trends of interest in Table 2 are the tendency of the half-mass radius to increase with increasing small-scale power and also with increasing rotational energy. Figure 4a shows the correlation of half-mass radius with the amplitude of the small-scale power for both  $n = 0$  models and  $n = -2.5$  models. Figure 4b shows the half-mass radius plotted against the initial  $T/W$ . Contrary to previous results (McGlynn 1984; May & van Albada 1984; Aguilar & Merritt 1989), the density profiles seem to be influenced by the initial amplitude of the small-scale power not just by the initial  $T/W$ . Furthermore, by comparing  $n = 0$  models with  $n = -2.5$  models in Figure 4a, the initial  $T_{\text{rand}}/W$  is not as important in determining the density profiles as the amplitude of the small-scale power at the  $k = 1$  mode. In addition, the fit parameters in Table 2 seem to depend mostly on the initial small-scale power amplitude and initial rotation velocity and not on the slope of the power spectrum.

Finally, there does not appear to be any clear correlation between the core radius and any of the initial parameters. Recalling that the gravitational softening length is  $\epsilon = 0.06$  and that the gravitational force law is Newtonian only beyond

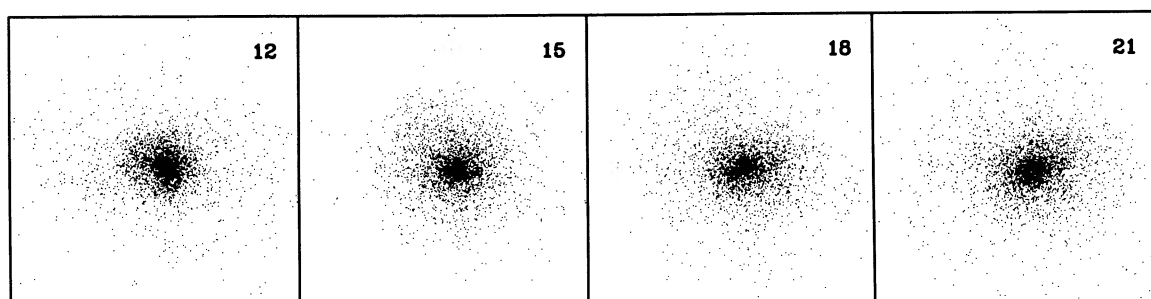
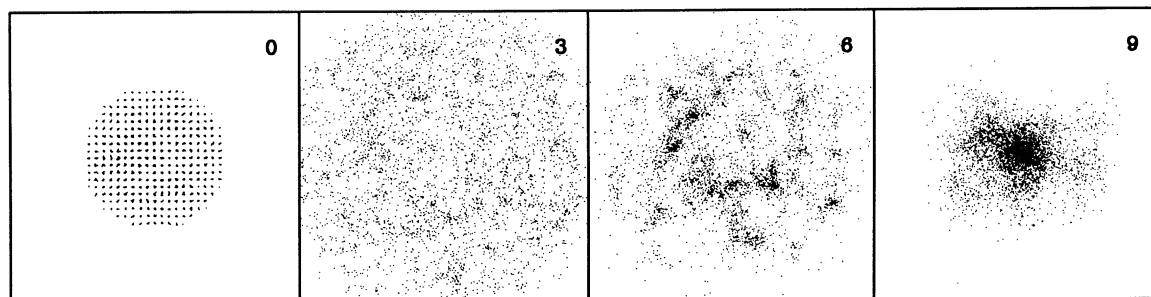


FIG. 1a

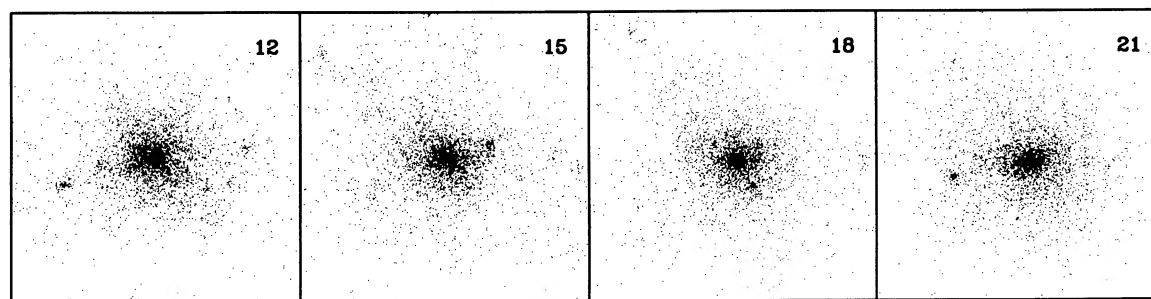
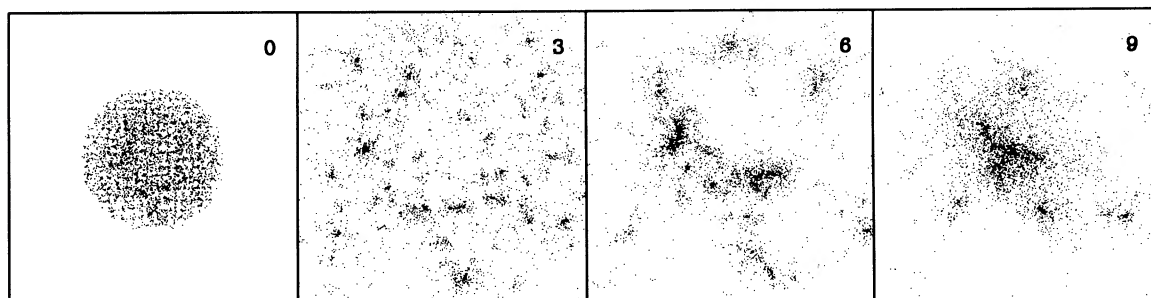


FIG. 1b

FIG. 1.—(a) Collapse of a system in Hubble flow with initial rotation  $\omega = 0.2$ . Power spectrum has slope  $n = 0$ . This is the lowest amplitude run. Time is shown in the upper right corner of each frame and is measured in units of the natural system time. Frames are four units across. (b) Same as (a) but for the highest amplitude run.

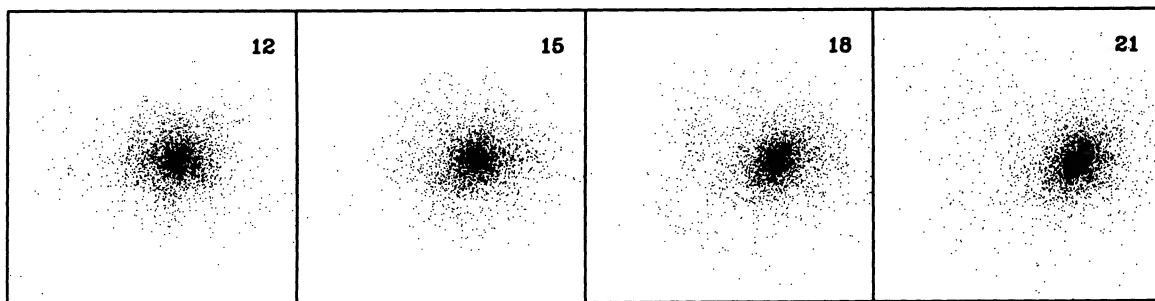
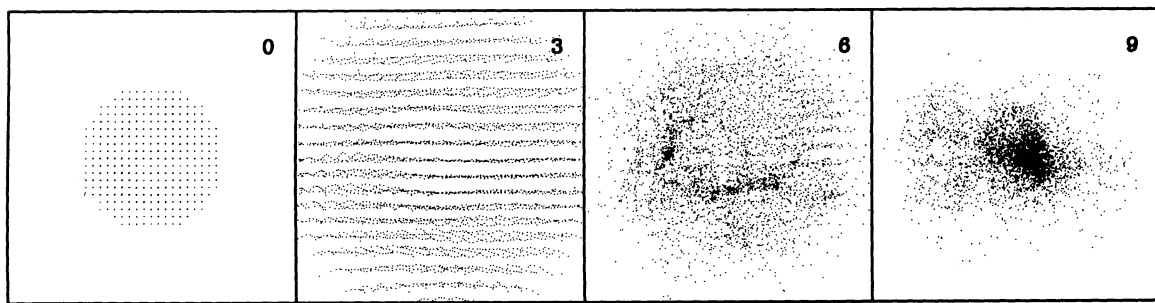


FIG. 2a

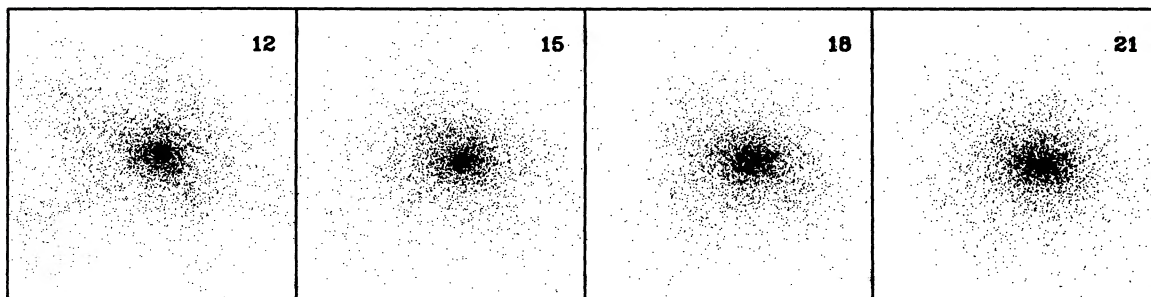
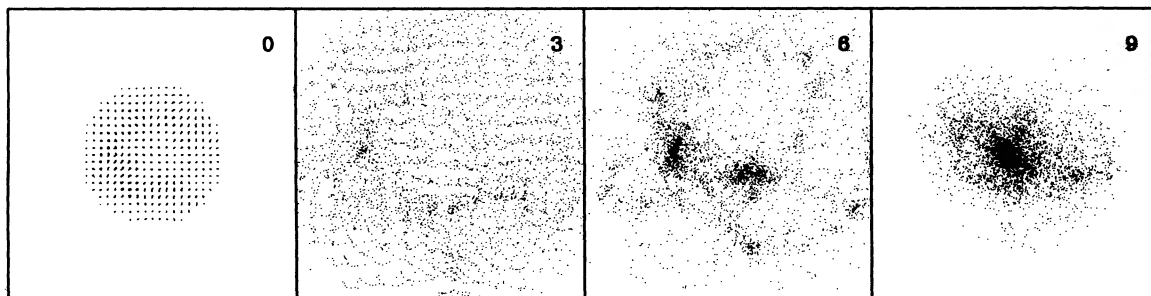


FIG. 2b

FIG. 2.—(a) Same as Fig. 1a but for  $n = -2.5$ . (b) Same as (a) but for the highest amplitude run.

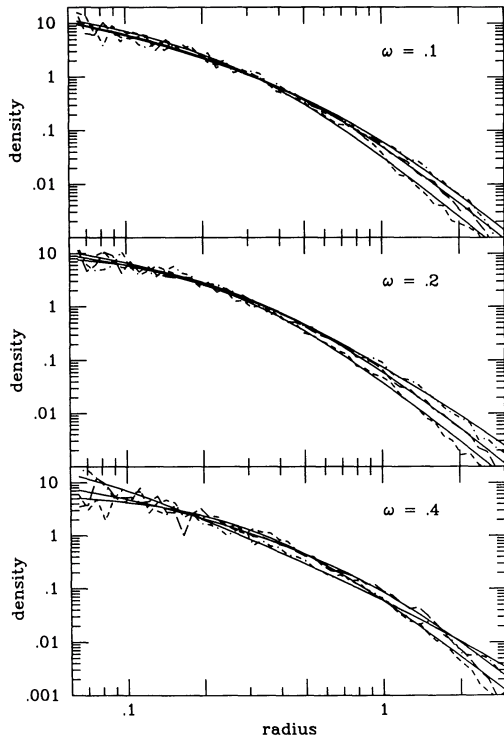


FIG. 3a

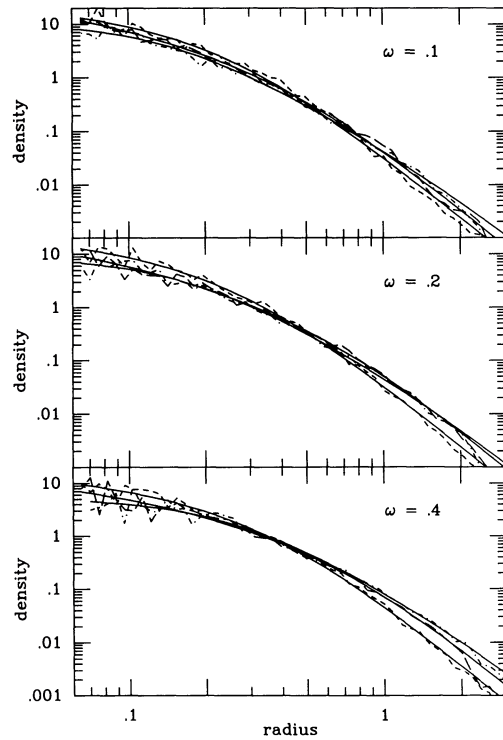


FIG. 3b

FIG. 3.—(a) Density plotted vs. radius for the  $n = 0$  runs. Short-dashed lines refer to the lowest amplitude runs, long-dashed lines to the intermediate amplitude runs, dot-dashed lines to the highest amplitude runs, and solid lines to the best-fit Jaffe model. The  $\omega$ 's refer to initial rotation. (b) Same as (a) but for  $n = -2.5$ .

two smoothing lengths, it is unclear if any of the density profiles have a core radius at all. The only runs where a reasonable case could be made for a core-radius are runs 7a and 9b.

Figures 5a and 5b show the dynamical circular velocity  $[(M(r)/r)^{1/2}]$  plotted as a function of radius for the  $n = 0$  and  $n = -2.5$  models, respectively. All the rotation curves rise rapidly to their peak velocity at a radius of  $\sim 0.3$ , beyond

which they start to drop slowly. Most remain flat out to a radius of 0.7 and some are almost flat out to 1.3 radius units. For runs with a smaller initial rotation and a smaller initial amplitude of small-scale fluctuations the rotation curves tend to fall off more quickly, without as much of a flat portion. The only notable difference between the  $n = 0$  and  $n = -2.5$  runs is that the low-amplitude runs have rotation curves which are

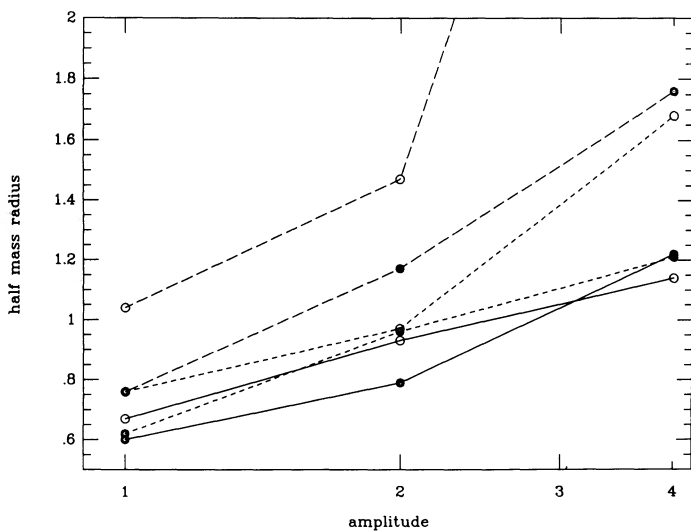


FIG. 4a

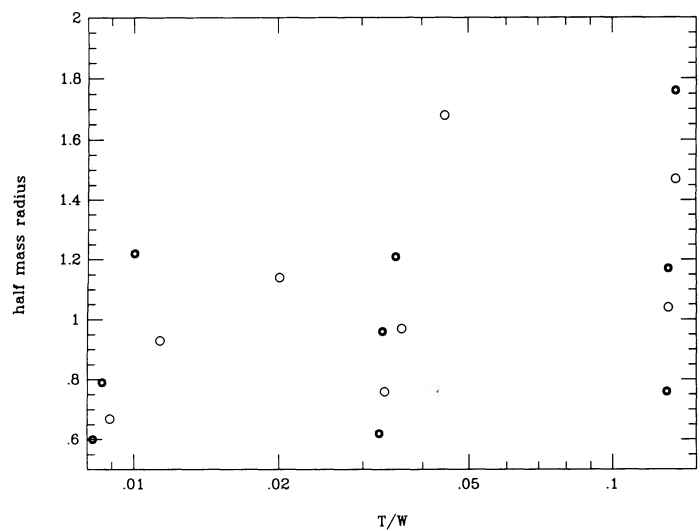


FIG. 4b

FIG. 4.—(a) Correlation between the half mass radius and the amplitude of small-scale power. Open circles represent  $n = 0$  runs and stars represent  $n = -2.5$  runs. Solid lines refer to  $\omega = 0.1$ , short-dashed lines to  $\omega = 0.2$ , and long-dashed lines to  $\omega = 0.4$ . (b) Correlation between the half mass radius and the initial  $T/W$ . Open circles represent  $n = 0$  runs and stars represent  $n = -2.5$  runs.

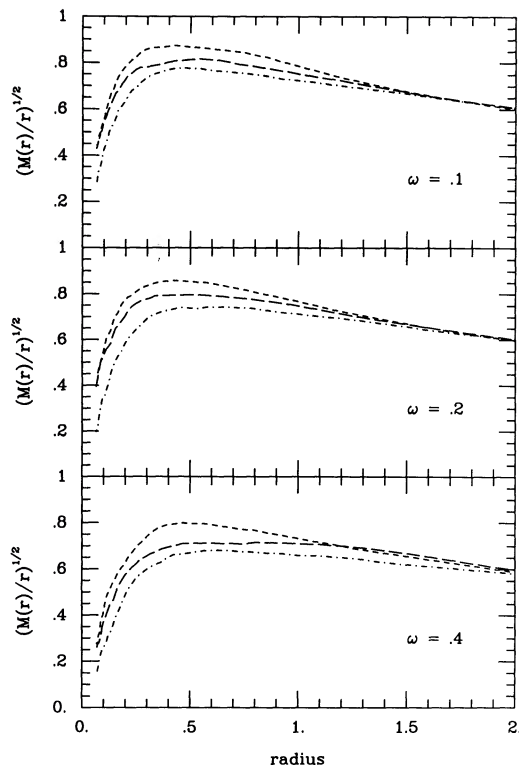


FIG. 5a

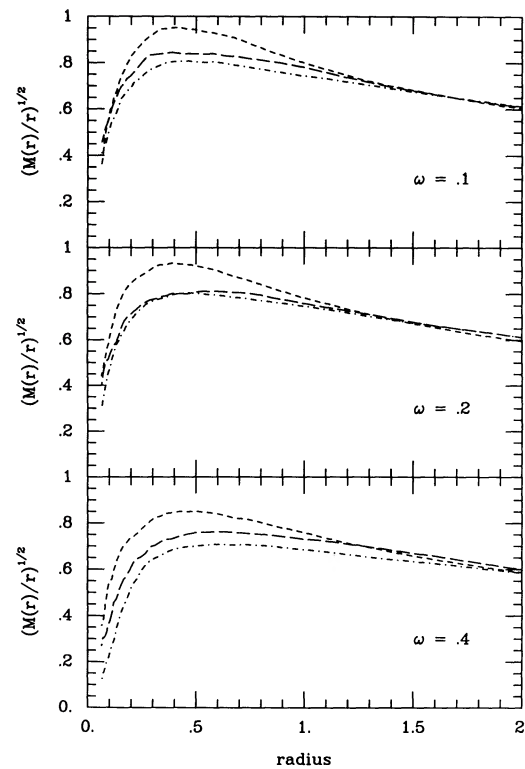


FIG. 5b

FIG. 5.—(a) Circular velocity plotted vs. radius for the  $n = 0$  runs. Short-dashed lines refer to the lowest amplitude runs, long-dashed lines to the intermediate amplitude runs, and dot-dashed lines to the highest amplitude runs. The  $\omega$ 's refer to initial rotation. (b) Same as (a) but for  $n = -2.5$ .

more sharply peaked in the  $n = -2.5$  models and have almost no flat portion at all.

### 3.3. The Shapes

The axis ratios of each run are determined at the half-mass radius. The axis ratios  $b/a$  and  $c/a$  are shown in Table 3, top, for the  $n = 0$  models and in Table 3, bottom, for the  $n = -2.5$  models. Depending on projection, these models have ellipticities ranging from 0.07 to 0.57 for the  $n = 0$  runs and from 0.04 to 0.54 for the  $n = -2.5$  runs. Also shown in these tables is the quantity  $\tau$  which is defined to be  $(b - c)/(a - c)$ . Objects with prolate shapes have  $\tau \approx 0$ , oblate objects have  $\tau \approx 1$ , and objects with intermediate values of  $\tau$  are triaxial. Runs 2a, 3a, 5a, and 6a are nearly prolate, runs 1a, 5b, and 6b are nearly oblate, and the rest of the runs are triaxial. The shapes do not appear to have any monotonic correlation with any of the initial parameters, but a qualitative trend should be noted: if the energy in the small-scale power is more important than the rotation energy prolate shapes result, and if the energy in the small-scale power is less important, oblate or triaxial shapes result.

### 3.4. Kinematic Properties

Since it is not possible to determine the individual components of the kinetic energy tensor accurately with only 4000 particles the following approach was developed. First, the particles are placed in concentric cylindrical bins, logarithmically spaced in radius, oriented with the axes of the cylinders parallel to the angular momentum axis of the system, and centered on the system's center of mass. All particles with  $\zeta \leq 2$  are

included and the shape of the ellipsoid is determined at  $\zeta = 2$ . As mentioned above, the density is found to rapidly decrease beyond a  $\zeta$  of two in most runs. In each bin, the mass-weighted average rotational velocity is determined and subtracted from each particle. Once this net rotation is removed the velocity dispersion is calculated along the  $x$ ,  $y$ , and  $z$  axes in a coordi-

TABLE 3  
AXIS RATIOS

Run	$b/a$	$c/a$	$\tau$
<i>n = 0</i> Runs			
1a .....	0.93	0.70	0.77
2a .....	0.63	0.58	0.12
3a .....	0.80	0.71	0.31
4a .....	0.87	0.65	0.63
5a .....	0.55	0.48	0.13
6a .....	0.58	0.53	0.11
7a .....	0.79	0.52	0.56
8a .....	0.68	0.43	0.44
9a .....	0.84	0.56	0.64
<i>n = -2.5</i> Runs			
1b .....	0.84	0.69	0.48
2b .....	0.89	0.74	0.58
3b .....	0.85	0.67	0.55
4b .....	0.78	0.63	0.41
5b .....	0.96	0.70	0.87
6b .....	0.96	0.72	0.86
7b .....	0.69	0.52	0.35
8b .....	0.64	0.46	0.33
9b .....	0.72	0.48	0.46

TABLE 4  
KINEMATIC PROPERTIES

Run	$b/a$	$c/a$	$V_x$	$V_y$	$V_z$	$\sigma_x$	$\sigma_y$	$\sigma_z$	Angle
$n = 0$ Runs									
1a	0.93	0.76	-0.003	-0.039	0.039	0.22	0.25	0.18	12
2a	0.82	0.70	0.024	-0.029	0.041	0.23	0.19	0.16	26
3a	0.73	0.67	0.028	0.033	0.055	0.21	0.17	0.16	18
4a	0.89	0.72	0.002	0.059	0.061	0.21	0.22	0.18	0
5a	0.78	0.61	0.032	-0.051	0.052	0.23	0.18	0.16	27
6a	0.63	0.59	0.010	0.059	0.075	0.22	0.16	0.15	7
7a	0.84	0.57	-0.029	0.047	0.11	0.22	0.18	0.14	17
8a	0.73	0.53	-0.014	0.079	0.078	0.20	0.17	0.12	5
9a	0.80	0.54	0.025	0.050	0.10	0.15	0.18	0.13	10
$n = -2.5$ Runs									
1b	0.90	0.72	0.037	0.014	0.050	0.27	0.25	0.21	25
2b	0.90	0.72	0.019	-0.042	0.062	0.22	0.21	0.18	16
3b	0.95	0.73	0.036	0.031	0.059	0.17	0.22	0.16	25
4b	0.91	0.71	0.040	-0.056	0.051	0.25	0.25	0.21	26
5b	0.93	0.66	-0.004	0.059	0.055	0.20	0.21	0.15	3
6b	0.93	0.72	0.041	0.047	0.063	0.20	0.21	0.16	25
7b	0.88	0.61	-0.003	0.038	0.12	0.20	0.25	0.16	4
8b	0.81	0.57	0.024	-0.009	0.090	0.22	0.17	0.14	14
9b	0.72	0.48	-0.017	0.011	0.082	0.20	0.16	0.12	11

nate system where the moment of inertia tensor is diagonal. Additionally, the mass-weighted rotation is calculated around these same axes without the net rotation removed. The results of these calculations are presented in Table 4, top, for the  $n = 0$  models and in Table 4, bottom, for the  $n = -2.5$  models. Also shown in this table are the axis ratios  $b/a$  and  $c/a$  for the particles within  $\zeta = 2$ .

Although the largest rotational motion is around the short axis of the system, there is also substantial rotation around the other axes. This may imply that, in addition to net streaming within the system, the ellipsoidal systems are tumbling in space. Additionally, if a galaxy actually rotated on cylinders, and one were to place a "slit" along the projected major axis

to determine the rotational velocity, a smaller velocity would be obtained than if the slit were oriented at an angle to the major axis. The angle between the major axis and a slit oriented to obtain the maximum value of the rotational velocity is also shown in Table 4, assuming that the projection is along the intermediate axis of the system.

One can use this kinematic information to determine if the shapes of the systems can be maintained through rotation. In Figure 6a values of  $v/\sigma$  are plotted against projected ellipticity. Each run is represented by three points: one for each projection along the three principal axes. The velocity that is used is the one that would be obtained by placing a slit along the major axis of the projected system. Figure 6b shows the same

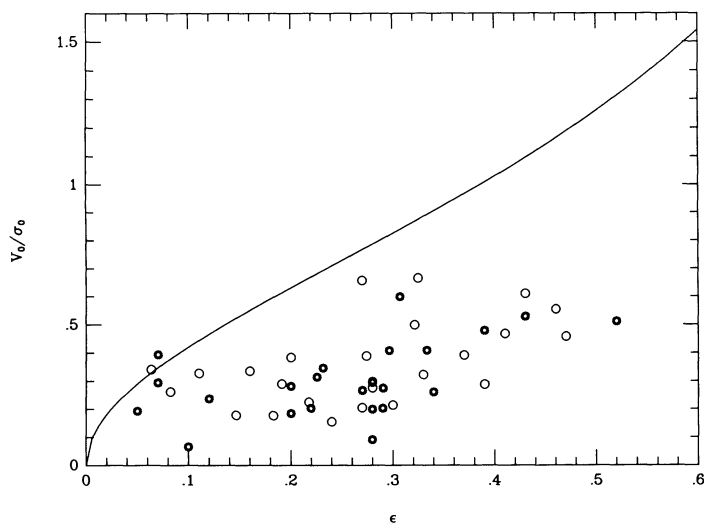


FIG. 6a

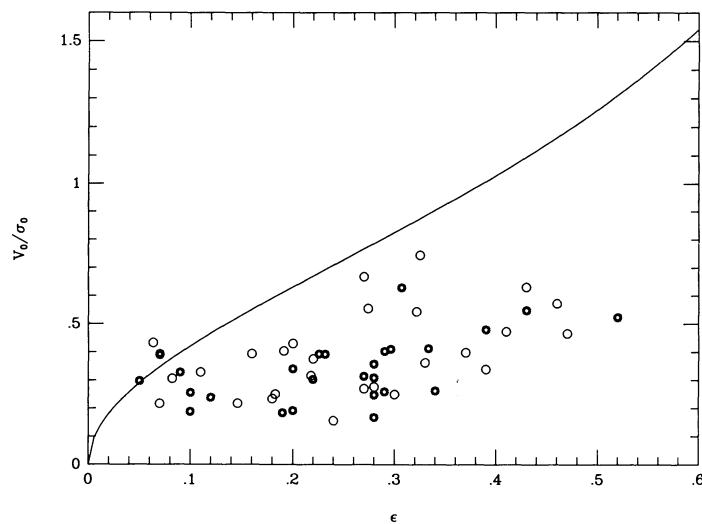


FIG. 6b

FIG. 6.—(a)  $V_0/\sigma_0$  plotted vs. projected ellipticity.  $V_0$  is the projected velocity along the major axis. Solid line is the theoretically predicted curve for an oblate rotator. Open circles represent  $n = 0$  runs and stars represent  $n = -2.5$  runs. (b) Same as (a) except  $V_0$  is now the projected velocity along a "slit" oriented to obtain the maximum projected velocity.

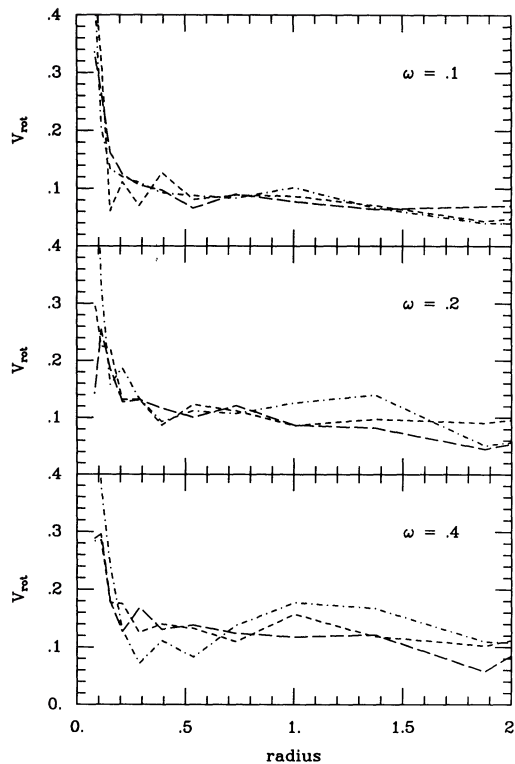


FIG. 7a

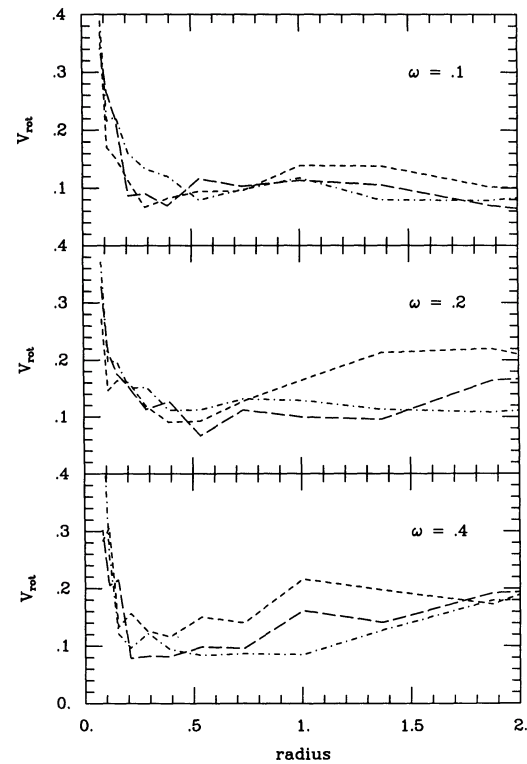


FIG. 7b

FIG. 7.—(a) Actual rotation velocity plotted vs. radius for the  $n = 0$  runs. Short-dashed lines refer to the lowest amplitude runs, long-dashed lines to the intermediate amplitude runs, and dot-dashed lines to the highest amplitude runs. The  $\omega$ 's refer to initial rotation. (b) Same as (a) but for  $n = -2.5$ .

information but the velocity used is the one that would be obtained by orienting the slit at the angle maximizing the rotational velocity. In both figures the open circles refer to  $n = 0$  models and the stars refer to  $n = -2.5$  models. The solid line shows the value of  $v/\sigma$  that would be required for a given ellipticity if the shape were supported through rotation alone (Binney 1978). It is immediately apparent that the shapes cannot be maintained by rotation alone and must be supported through an anisotropic velocity dispersion. From Table 4, the velocity dispersion is anisotropic, with the smallest dispersion along the shortest axis. There is also no significant segregation of the  $n = 0$  models and the  $n = -2.5$  models in Figures 6.

Figures 7a and 7b show rotation curves for the  $n = 0$  and  $n = -2.5$  models, respectively. These curves are obtained by binning the particles in concentric cylinders logarithmically spaced in radius and then determining the mass-weighted rotation velocity in each bin. The rotation curves are flat and there is a slight trend toward increasing rotational velocity in systems with larger initial rotation. The rotation velocities are much less than the dynamically determined circular velocities at these radii.

#### 4. DISCUSSION

Several things have been learned from these simulations. Some of the most interesting concern the form of the density profiles. Jaffe density profiles are produced for a wide range of initial conditions, with differing amounts of small-scale inhomogeneities and initial rotations. When viewed in projection these profiles roughly follow a de Vaucouleurs  $R^{1/4}$  surface

density profile. The detailed structure of the density profiles for a given initial rotation is determined by the amplitude of the small-scale power in the  $k = 1$  mode and does not appear to be much affected by power at smaller scales. This implies that it is only the largest subclumps that are important in the violent relaxation that ensues when the system collapses and virializes. In retrospect, this behavior should have been anticipated, since the largest subclumps will be the most important in producing the rapidly varying potential that is responsible for violent relaxation.

Two other interesting phenomena are also seen. Some of the final equilibrium states have a prolate shape while others are either oblate or triaxial. In the systems where rotation is more important than the small-scale power, oblate or triaxial systems result, while in systems where small-scale power is more important than rotation, the final systems are prolate. Other authors (e.g., Aguilar & Merritt 1989) have argued that in their collapse simulations the radial orbit instability determines the final shape of the system. Systems with cool initial conditions ( $T/W < 0.05$ ) tend to be prolate while warmer systems tend to be oblate. No such trends are found here. This is probably because the collapses resulting from the self-consistent initial conditions used in this study resemble multiple merger events, while nearly spherical homogeneous collapse is necessary for the radial orbit instability to be important.

The final equilibrium states are also found to be rotating with flat rotation curves which have amplitudes that are almost independent of the initial rotational velocity. Other authors (e.g., Zurek, Quinn, & Salmon 1988) find that in

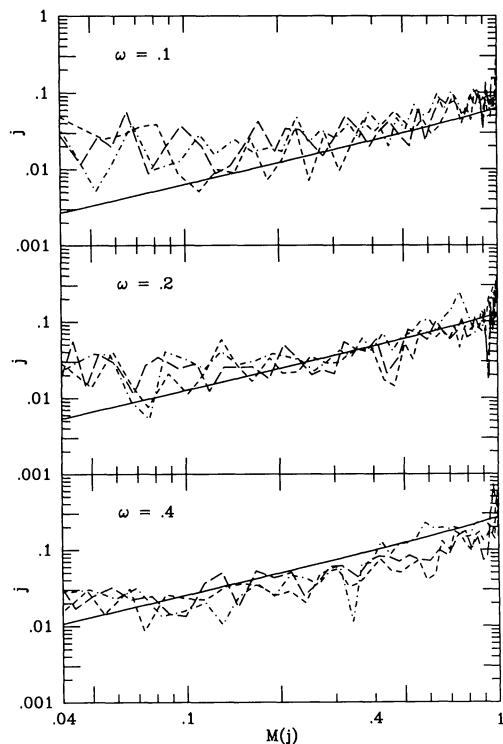


FIG. 8a

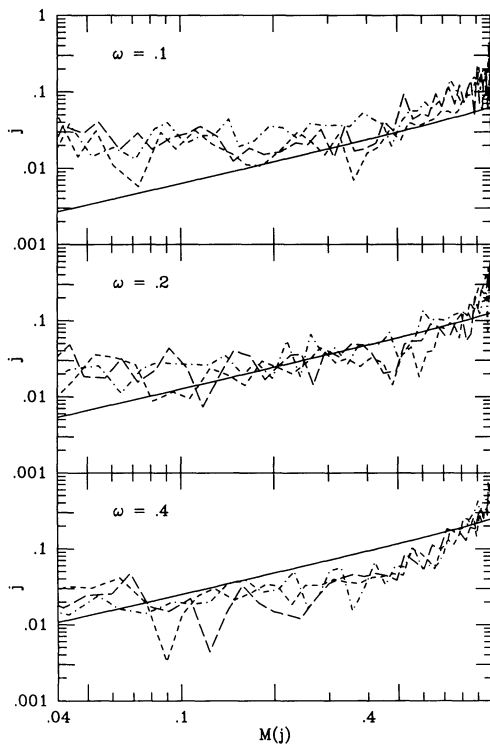


FIG. 8b

FIG. 8.—(a) Specific angular momentum plotted vs.  $M(j)$  for the  $n = 0$  runs. Short-dashed lines refer to the lowest amplitude runs, long-dashed lines to the intermediate amplitude runs, and dot-dashed lines to the highest amplitude runs. The solid line refers to the initial conditions and the  $\omega$ 's refer to initial rotation. (b) Same as (a) but for  $n = -2.5$ .

merger events angular momentum is transported quite efficiently. It could be possible, therefore, that these flat rotation curves are the result of angular momentum transport that acted during the collapse. Figures 8 show the specific angular momentum,  $j$ , plotted versus the mass that has specific angular momentum less than  $j$ ,  $M(j)$ , for the final equilibrium systems when binned on concentric cylinders. Ignoring the central areas where the gravitational potential is softened, the  $M(j)$ 's do not differ markedly from their original distributions, represented by solid lines in the figures, except in the highest initial rotation collapses with  $n = -2.5$ . Angular momentum transport, therefore, is not important in the majority of these collapses. The isolated nature of the perturbations studied here naturally prevents outer regions from transporting angular momentum outward, but it may have also affected angular momentum transport in the inner regions. It is nevertheless remarkable that angular momentum transport is negligible for over 70% of the mass, when the collapses are so violent and inhomogeneous.

There are two obvious physical applications for these simulations. On the one hand, they could represent the collapse and formation of dark matter halos in a hierarchical clustering cosmogony with a unit mass of  $7 \times 10^{11} M_{\odot}$ , implying a system mass of  $6.4 \times 10^{11} M_{\odot}$ , and unit length of 62.5 kpc. Values of  $\lambda$  that range from 0.02 to 0.1 are found for galactic halos in larger cosmological simulations (Barnes & Efstathiou 1987; Zurek, Quinn, & Salmon 1988). This is just the range covered in these simulations.

Simulations of dark halo formation with a bias of 2.5 are calculated by Frenk et al. (1988). The mass resolution in their

models is limited to  $6 \times 10^9 M_{\odot}$ , while in the simulations here the mass resolution limit is  $1.6 \times 10^8 M_{\odot}$ . The typical halo in their simulations, therefore, contains only  $\sim 100$  particles. Because of this poor resolution not much can be learned about the halos at radii where their dynamical effects are really observed. They find that rotation curves become flat at  $\sim 40$  kpc for systems of this mass and remain flat out to  $\sim 200$  kpc. This should be contrasted with the simulations in this paper where the rotation curves peak at 20 kpc but then remain flat only for the bias 2 and bias 1 models. Even then, they remain flat only out to  $\sim 45$ –60 kpc. The drop at larger radii is probably the result of using an isolated top-hat perturbation with no secondary infall. In fact, over 60% of the total bound simulation mass is typically within the radius where the rotation curves begin to fall, indicating that the simulation is “running out of mass.” The models in this paper, therefore, probably should not be trusted beyond  $\sim 50$  kpc.

Quinn, Salmon, & Zurek (1988) run simulations similar to those of Frenk et al. for various power-law slopes. They have slightly better resolution ( $\sim 100$ –1000 particles per halo) than Frenk et al. but the circular velocities of their systems are less than  $50 \text{ km s}^{-1}$  for  $n = -2.75$  models; far less than the  $\sim 180 \text{ km s}^{-1}$  in the models here. The circular velocities of their  $n = 0$  models are comparable to the current simulations, however. They find that the density profiles, and therefore the calculated circular velocity rotation curves, are dependent on the power-law slope of the density perturbations. For larger values of  $n$  (including  $n = 0$ ), the rotation curves do not remain flat but fall off gradually, whereas for lower values of  $n$  the rotation curves remain flat. Quinn et al. find similar trends in the actual mea-

sured rotation of their systems: trends that are absent in the current simulations. In addition, the current simulations find no major differences between the density profiles of the  $n = 0$  models and the  $n = -2.5$  models, and only slight differences are found in the rotation curves.

There are four possible explanations for these differences. First, the current simulations assume an isolated top-hat density profile and have no secondary infall. Although infall may affect only the outer parts of the systems, there is a possibility that even the innermost parts are affected. Second, because of the way that Quinn et al. normalize their spectrum there is a trend of maximum system circular velocity with  $n$ . The trends that they find may result from comparing inherently different systems, while in the current simulations the circular velocities are approximately independent of  $n$ . Third, in the current simulations angular momentum is added through solid body rotation, while in the Quinn et al. simulations the angular momentum is acquired naturally from tidal torquing which could change the results. Finally, there is the question of the differing resolution between the simulations. When considering the merger of clumps and their subsequent exchange of angular momentum, resolution could be very important. This would especially affect the measured rotation curves. Higher resolution allows one to study the central part of the halos. For example, in most of the current simulations, no core radius is found down to the simulation resolution of  $\sim 7$  kpc.

The other obvious application for the simulations in this paper is the dissipationless formation of elliptical galaxies. In this case the dissipationless material is stars that formed early in the collapse. The final virialized objects found here are similar to observed elliptical galaxies. They have surface density profiles that roughly follow a de Vaucouleurs  $R^{1/4}$  law, projected ellipticities comparable to those that are observed, and have kinematic properties similar to those of elliptical galaxies. These kinematic properties include the observed  $v/\sigma$  relation (Binney 1978), the observed flat rotation curves (Davies & Birkinshaw 1988), and the angles between the rotation axes and the projected minor axes (Davies & Birkinshaw 1988). The main difficulty with forming elliptical galaxies in

this manner is finding a way to efficiently turn the baryons into stars at an early epoch. Perhaps if stars form efficiently in the centers of the clumps, the final virialized objects would be similar. Such investigations will have to be done with computer codes that include gas dynamics (e.g., HK).

## 5. CONCLUSIONS

Dissipationless collapse with cosmologically realistic initial conditions more closely resembles a multiple merger event than the smooth collapse of a spherical top hat. The resulting density profiles are well described by a modified Jaffe model, which resembles a de Vaucouleurs  $R^{1/4}$  profile in projection. The quantitative shape of the density profile is most dependent on the amplitude of the small-scale power with almost no dependence on the power-law slope. This implies that it is the largest subclumps that dominate the violent relaxation process. The radial orbit instability appears unimportant in these collapses and the final shapes range from oblate to triaxial to prolate. The final shape seems to be related to the relative importance of the small-scale power and the solid body rotation in the initial conditions. With these more general initial conditions the initial  $T/W$  does not completely determine the final equilibrium state. The equilibrium systems are slowly rotating, with flat rotation curves (i.e., the actual rotation of the particles), and their shapes are supported through an anisotropic velocity dispersion.

The final equilibrium states closely resemble elliptical galaxies with projected ellipticities ranging from E1 to E6, lending support to the idea that elliptical galaxies formed through dissipationless collapse. The collapses could also represent galactic halo formation, but they probably cannot be trusted to very large radius due to the lack of secondary infall. This type of information will have to wait for even more realistic collapses of nonisolated perturbations.

I would like to thank Jim Gunn, Lars Hernquist, David Weinberg, Simon White, David Spergel, Kevin Long, and Man Hoi Lee for numerous discussions. This work was supported in part by a grant from the Pittsburgh Supercomputing Center and NSF grant AST 880013P.

## REFERENCES

- Aguilar, L., & Merritt, D. 1990, *ApJ*, 354, 33  
 Aguilar, L., Merritt, D., & Duncan, M. 1987, *IAUS* 127, Structure and Dynamics of Elliptical Galaxies, ed. T. de Zeeuw (Dordrecht: Reidel), p. 519  
 Barnes, J., & Efstathiou, G. 1987, *ApJ*, 319, 575  
 Barnes, J., & Hut, P. 1986, *Nature*, 324, 446  
 Binney, J. 1978, *MNRAS*, 183, 501  
 Bouvier, P., & Janin, G. 1970, *A&A*, 5, 127  
 Davies, R. L., & Birkinshaw, M. 1988, *ApJS*, 68, 409  
 Ewell, M. W. 1988, Ph.D. thesis, Princeton University  
 Frenk, C. S., White, S. D. M., Davis, M., & Efstathiou, G. 1988, *ApJ*, 327, 507  
 Frenk, C. S., White, S. D. M., Efstathiou, G., & Davis, M. 1990, *ApJ*, 351, 10  
 Gott, J. R. 1973, *ApJ*, 186, 481  
 Hénon, M. 1964, *Annd'Ap*, 27, 83  
 Hernquist, L. 1987, *ApJS*, 64, 715  
 Hernquist, L. 1990, *JCP*, 87, 137  
 Hernquist, L., & Katz, N. 1989, *ApJS*, 70, 419 (HK)  
 Jaffe, W. 1983, *MNRAS*, 202, 995  
 May, A., & van Albada, T. S. 1984, *MNRAS*, 209, 15  
 McGlynn, T. 1984, *ApJ*, 281, 13  
 Peebles, P. J. E. 1970, *AJ*, 75, 13  
 ———. 1971, *A&A*, 11, 377  
 ———. 1982, *ApJ*, 263, L1  
 Quinn, P. J., Salmon, J. K., & Zurek, W. H. 1986, *Nature*, 322, 329  
 Quinn, P. J., & Zurek, W. H. 1988, *ApJ*, 331, 1  
 van Albada, T. S. 1982, *MNRAS*, 201, 939  
 Zel'dovich, Ya. B. 1970, *A&A*, 5, 84  
 Zurek, W. H., Quinn, P. J., & Salmon, J. K. 1988, *ApJ*, 330, 519